Monthly Notices of the ROYAL ASTRONOMICAL SOCIETY

MNRAS **520,** 4000–4008 (2023) https://doi.org/10.1093/mnras/stad377
Advance Access publication 2023 February 2

THE THREE HUNDRED project: a machine learning method to infer clusters of galaxy mass radial profiles from mock Sunyaev–Zel'dovich maps

A. Ferragamo [1]★ D. de Andres [2,3]★ A. Sbriglio,[1] W. Cui [2,3,4] M. De Petris,[1] G. Yepes [2,3] R. Dupuis,[5] M. Jarraya,[5] I. Lahouli,[5] F. De Luca [6] G. Gianfagna[1,7] and E. Rasia [8,9]

[1]*Dipartimento di Fisica, Sapienza Università di Roma, Piazzale Aldo Moro 5, I-00185 Roma, Italy*
[2]*Departamento de Física Téorica, Facultad de Ciencias, Universidad Autónoma de Madrid, Módulo 8, E-28049 Madrid, Spain*
[3]*Centro de Investigación Avanzado en Física Fundamental (CIAFF), Facultad de Ciencias, Universidad Autónoma de Madrid, E-28049 Madrid, Spain*
[4]*Institute for Astronomy, University of Edinburgh, Edinburgh EH9 3HJ, UK*
[5]*EURANOVA, Rue Emile Francqui 4, 1435 Mont-Saint-Guibert, Belgium*
[6]*Dipartimento di Fisica, Università di Roma Tor Vergata, Via della Ricerca Scientifica 1, I-00133 Roma, Italy*
[7]*INAF – Istituto di Astrofisica e Planetologia Spaziali, Via Fosso del Cavaliere 100, I-00133 Roma, Italy*
[8]*IFPU – Institute for Fundamental Physics of the Universe, Via Beirut 2, I-34014 Trieste, Italy*
[9]*INAF – Osservatorio Astronomico di Trieste, Via Tiepolo 11, I-34131 Trieste, Italy*

Accepted 2023 January 27. Received 2023 January 27; in original form 2022 July 27

ABSTRACT

We develop a machine learning algorithm to infer the three-dimensional cumulative radial profiles of total and gas masses in galaxy clusters from thermal Sunyaev–Zel'dovich effect maps. We generate around 73 000 mock images along various lines of sight using 2522 simulated clusters from THE THREE HUNDRED project at redshift $z < 0.12$ and train a model that combines an auto-encoder and a random forest. Without making any prior assumptions about the hydrostatic equilibrium of the clusters, the model is capable of reconstructing the total mass profile as well as the gas mass profile, which is responsible for the Sunyaev–Zel'dovich effect. We show that the recovered profiles are unbiased with a scatter of about 10 per cent, slightly increasing towards the core and the outskirts of the cluster. We selected clusters in the mass range of $10^{13.5} \leq M_{200}/(h^{-1}\,\mathrm{M}_{\odot}) \leq 10^{15.5}$, spanning different dynamical states, from relaxed to disturbed haloes. We verify that both the accuracy and precision of this method show a slight dependence on the dynamical state, but not on the cluster mass. To further verify the consistency of our model, we fit the inferred total mass profiles with a Navarro–Frenk–White model and contrast the concentration values with those of the true profiles. We note that the inferred profiles are unbiased for higher concentration values, reproducing a trustworthy mass–concentration relation. The comparison with a widely used mass estimation technique, such as hydrostatic equilibrium, demonstrates that our method recovers the total mass that is not biased by non-thermal motions of the gas.

Key words: methods: numerical – galaxies: clusters: general – cosmology: theory.

1 INTRODUCTION

Small density fluctuations in the early Universe were the seeds for structure formation. The latest stage of structure evolution is characterized by the formation of clusters of galaxies. Galaxy clusters are the largest gravitationally bound structures in the Universe, reaching a mass of a few $10^{15}\,h^{-1}\,\mathrm{M}_{\odot}$. The majority of this mass, about 80 per cent, corresponds to dark matter (DM), 12 per cent is diffused hot gas, i.e. the intracluster medium (ICM), and the 8 per cent are galaxies within the ICM (see Kravtsov & Borgani 2012, for a review). The abundance of galaxy clusters as a function of the mass and redshift, i.e. the halo mass function, is crucial for constraining cosmological parameters (e.g. Allen, Evrard & Mantz 2011; Pratt et al. 2019).

However, the DM component cannot be directly observed. On the contrary, the baryons could be revealed in the optical band via star/galaxy emission, at infrared wavelengths with the dust emission, in the X-ray band via bremsstrahlung emission, or at sub/millimetre wavelengths via the Sunyaev–Zeldovich (SZ; Sunyaev & Zeldovich 1970) effect. Through the information that the baryon component gives us, it is therefore possible to have some hints on the cluster's total mass. Common approaches exploit: (1) X-ray and SZ observations to recover cluster potential well from the ICM distribution under the assumption of hydrostatic equilibrium (HE), (2) mapping background lensed objects revealing cluster mass distorting power, and (3) galaxy member kinematics indicating potential well (see Pratt et al. 2019, for a review). Due to the basic assumptions and measurement difficulties of each of the methods, the inferred mass could be affected by biases. These biases are commonly quantified in hydrodynamical simulations comparing the true and method-derived masses. In a recent review by Gianfagna et al. (2021), the mass, estimated with the HE model in synthetic clusters, is from a minimum of 10 per cent to a maximum of 20 per cent lower than the real value. Consistent results

★ E-mail: ferragamoantonio@gmail.com (AF); daniel.deandres@uam.es (DdeA)

© 2023 The Author(s)
Published by Oxford University Press on behalf of Royal Astronomical Society

Downloaded from https://academic.oup.com/mnras/article/520/3/4000/7024857 by Universita' degli Studi Roma La Sapienza user on 19 June 2023

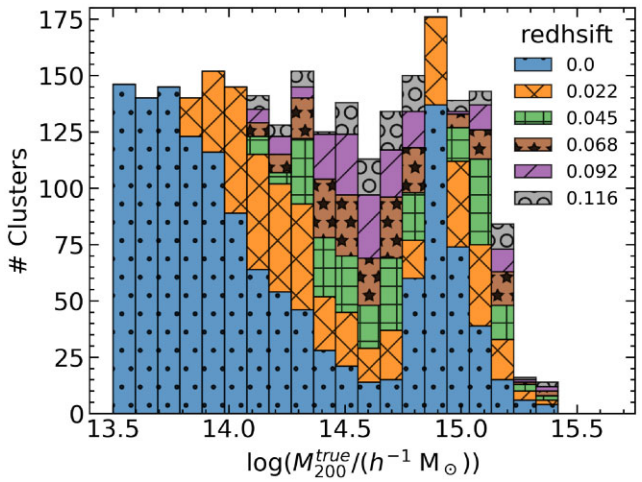

Figure 1. Mass distribution of clusters at the selected redshifts. The sample is first selected at redshift $z = 0$ (blue bars), and then it is complemented with clusters at the other redshifts (represented by the colours defined in the legend) to make it homogeneous.

are also derived in clusters from THE THREE HUNDRED simulations (Gianfagna et al. 2022). The origin of this bias is still not totally constrained as well as its dependence on the cluster properties, mainly the dynamical state, and the redshift. Non-thermal pressure support due to different gas motion components (Lau, Kravtsov & Nagai 2009) could have an impact on the cluster mass budget. Moreover, the bias seems to be affected by the cluster relaxation state (Ansarifard et al. 2020; Gianfagna et al. 2022). More intriguing is the bias dependence on the redshift. While simulations agree on a negligible dependence (Henson et al. 2016; Gianfagna et al. 2022), observational data support that the estimated masses are more biased at higher redshift (Sereno & Ettori 2017; Wicker et al. 2022), but probably this can be due to observational mass selection effect.

Therefore, even if the cluster total mass is a powerful tool to constrain the evolution of the Universe, inaccurate estimates of this quantity make a large impact in the inference of the cosmological parameters (Pratt et al. 2019; Salvati, Douspis & Aghanim 2020).

Recently, machine learning (ML) models have started to be applied for estimating the cluster mass from mock multiband images (Ntampaka et al. 2015, 2016, 2017). More recently, Ho et al. (2019) suggested that ML algorithms can also be used to assess the effect of interlopers in the dynamical cluster mass estimates. Exploiting the power of convolutional neural networks (CNNs), this methodology is playing an important role in the analysis of synthetic observations of X-ray (Ntampaka et al. 2019) and SZ (Gupta & Reichardt 2020; Yan et al. 2020; Gupta & Reichardt 2021). Moreover, it has been recently applied for the first time, on real cluster observations from Planck Compton-y parameter maps (de Andres et al. 2022). By considering no physical assumptions about the gas in clusters, this technique can ideally infer unbiased mass values for real clusters.

In this work, we present a combination of deep learning architecture, followed by an ML regression method that has been developed in order to infer the total mass radial profile of clusters extracted from THE THREE HUNDRED simulations. We take as inputs a large sample of mock SZ maps quantified in terms of the Compton-y parameter. Moreover, in order to obtain an independent estimate of the gas fraction, we designed our machinery to infer simultaneously the cluster gas mass radial profile.

This paper is organized as follows: In Section 2, we introduce the simulated data set, based on a cluster sample extracted from THE THREE HUNDRED project, and the mock SZ maps.

In Section 3, we briefly describe the deep learning architecture, based on an auto-encoder that is used to extract features from SZ maps and the random forest (RF) regression algorithm that performs the mass profile inference. The results of our study are reported in Section 4 where we also analyse the performance of our method. Finally, in Section 6 we compare our results with more classical approaches based on the HE approximation and we summarize our main conclusions in Section 7.

2 DATA SET

2.1 Simulation

This study is based on synthetic clusters generated in THE THREE HUNDRED project, first introduced in Cui et al. (2018). This consists in a set of zoomed hydrodynamic simulations of 324 spherical regions of 15 h^{-1} Mpc radius centred on the most massive clusters ($M_{\rm vir} > 8 \times 10^{14}\ h^{-1}\,{\rm M}_\odot$, at $z = 0$) identified within the DM-only MultiDark Planck 2 simulation (MDPL2; Klypin et al. 2016) by the ROCKSTAR halo finder (Behroozi, Wechsler & Wu 2013). The MDPL2 simulation is a comoving volume of $(1\,h^{-1}\,{\rm Gpc})^3$ containing 3840^3 DM particles of mass $1.5 \times 10^9\ h^{-1}\,{\rm M}_\odot$ and implements the Planck cosmology ($\Omega_{\rm m} = 0.307$, $\Omega_{\rm b} = 0.048$, $\Omega_\Lambda = 0.693$, $h = 0.678$, $\sigma_8 = 0.823$, and $n_{\rm s} = 0.96$; Planck Collaboration XIII 2016). To resimulate each THE THREE HUNDRED region with the full baryonic physics, the particles within the sphere of radius 15 h^{-1} Mpc were mapped back to the initial conditions and were splitted into DM ($M_{\rm DM} = 1.27 \times 10^9\ h^{-1}\,{\rm M}_\odot$) and gas ($M_{\rm gas} = 2.36 \times 10^8\ h^{-1}\,{\rm M}_\odot$) particles according to the universal baryon fraction of the Universe as estimated by *Planck*, preserving the original mass resolution. The remaining particles outside the zoomed regions were resampled as low-resolution particles in order to take into account the large-scale gravitational tidal field and reduce the computational cost. The hydrodynamical resimulations were performed by using the TREEPM + SPH GADGET-X code, a modified version of the GADGET3 code that includes an improved smoothed particle hydrodynamics (SPH) scheme to account for the gas dynamics of the baryonic component in the simulations (Springel 2005; Beck et al. 2016). The code also includes metal-dependent cooling as described in Tornatore et al. (2007). Star formation and supernova heating are modelled following the scheme of Springel & Hernquist (2003). Moreover, the effects of active galactic nucleus (AGN) feedback via gas accretion on to supermassive black holes are also taken into account as described in Steinborn et al. (2015).

Each of the 324 resimulated regions was then analysed by using the Amiga's halo finder (AHF; Knollmann & Knebe 2009). It detects all haloes by identifying the local peaks in the total density field interpolated from particles on to a hierarchical mesh structure. It then estimates R_{200} of each halo, as the radius at which the density of the object reaches 200 times the critical density of the Universe $\rho_{\rm c}$, and M_{200}, as the mass of all the particles dynamically bounded to the cluster that lies within this radius. Hereafter, we refer to these quantities as $R_{200}^{\rm true}$ and $M_{200}^{\rm true}$.

The sample used in this work is made of 2522 clusters uniformly distributed within the mass interval $10^{13.5} \leq M_{200}/(\,h^{-1}\,{\rm M}_\odot) \leq 10^{15.5}$ at six nearby redshifts, from $z = 0$ to 0.116, in order to have an almost homogeneously mass populated sample. Note, however,

Downloaded from https://academic.oup.com/mnras/article/520/3/4000/7024857 by Universita' degli Studi Roma La Sapienza user on 19 June 2023

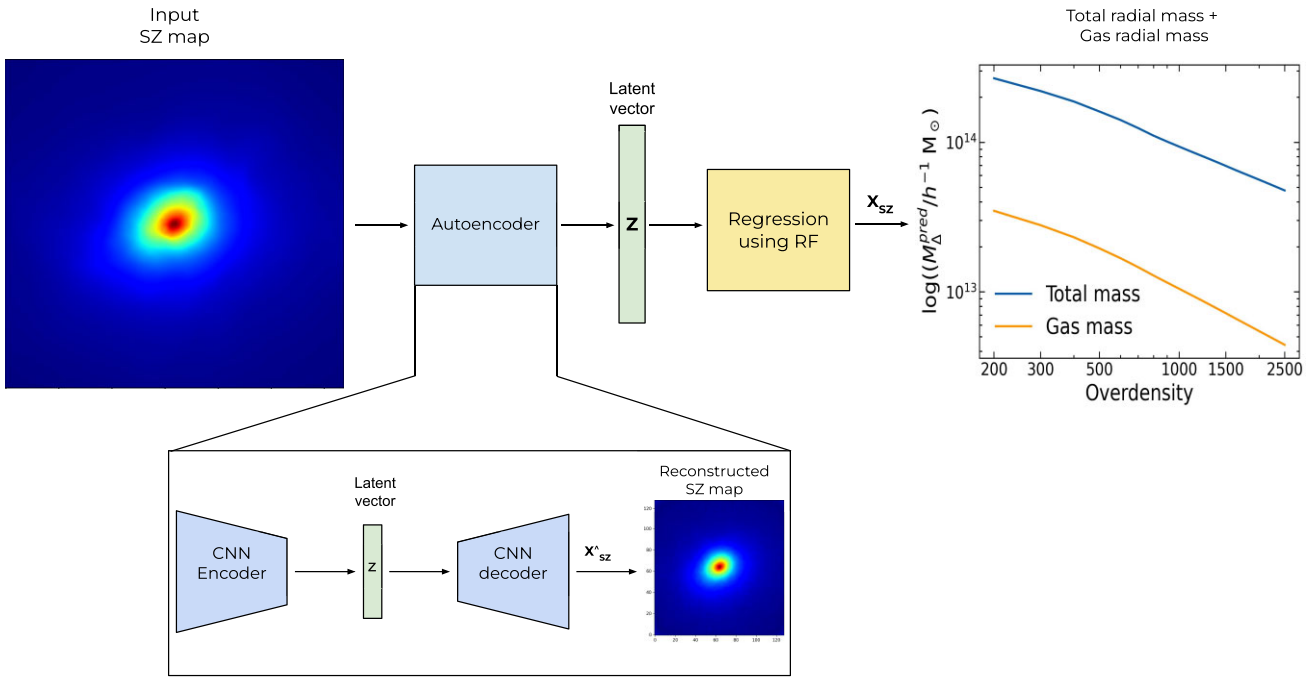

Figure 2. The 3D radial mass profile inference architecture using the auto-encoder plus the RF. The auto-encoder encrypts the input SZ map in a latent vector. The latter is then used as input for the RF regressor.

that there must be always fewer haloes in the larger mass range (see Fig. 1).

2.2 Cluster mass radial profiles

For each cluster, we extract the cumulative three-dimensional (3D) radial profiles of the total mass and the gas mass. These profiles are obtained by summing up the mass of all the particles within concentric spheres, centred in the AHF position corresponding to the highest density peak, up to $r = 2R_{200}$. We have interpolated the total mass profiles at fixed overdensities. We selected 24 linearly spaced overdensities, Δ from 200 to 2500, to homogeneously sample the profiles. This profile sampling allows us to predict the mass at overdensities that are commonly used in literature, such as M_{200}, M_{500}, and M_{2500}. With this approach, we differ and extend the previous work in literature that estimates the cluster mass always at a specific single aperture. M_{200} was derived in Gupta & Reichardt (2020) from simulated SZ map, Yan et al. (2020) by using optical, X-ray and SZ images generated from BAHAMAS simulation while Ntampaka et al. (2019) trained a CNN model to recover M_{500} from Illustris TNG X-ray mock images.

The SZ (Sunyaev & Zeldovich 1970) effect consists of an inverse Compton scattering of cosmic microwave background (CMB) photons on the hot plasma of the ICM. This leaves a specific fingerprint on the CMB at the position of a galaxy cluster, shifting photons energy to higher frequencies. The observable of the SZ effect is the Compton-y parameter defined as

$$y = \frac{\sigma_{\rm T} k_{\rm B}}{m_{\rm e} c^2} \int n_{\rm e} T_{\rm e} {\rm d}l, \tag{1}$$

where $\sigma_{\rm T}$, $k_{\rm B}$, c, and $m_{\rm e}$ are the Thomson cross-section, the Boltzmann constant, the speed of light, and the electron mass at rest, respectively. Whereas, $n_{\rm e}$, the electron number density, and $T_{\rm e}$, the electron temperature, are integrated along the line of sight, dl.

In numerical simulation the quantity $n_{\rm e}$ can be substituted with the discrete number of electrons in the gas particle $N_{\rm e}$, by assuming that $n_{\rm e} = N_{\rm e}/{\rm d}A/{\rm d}l$, where d$A$ is the projected area. Thus, the integral in the equation (1) can be replaced by the sum (Sembolini et al. 2013; Le Brun, McCarthy & Melin 2015):

$$y \simeq \frac{\sigma_{\rm T} k_{\rm B}}{m_{\rm e} c^2 d A} \sum_i N_{\rm e,i} T_{\rm e,i} W(r, hi), \tag{2}$$

where $W(r, h_i)$ is the projected SPH kernel adopted in simulation with the smoothing length h_i and used to spread each mass particle to the surrounding area. This equation is implemented in the public package PYMSZ (Baldi et al. 2018; Cui et al. 2018) that is used here to generate Compton-y parameter maps. For each map, gas particles inside a cube of side $2R_{200}$, centred in the cluster centre identified by AHF, are taken into consideration. The pixel size of each map is parametrized in terms of R_{200}, i.e. a $R_{200}xR_{200}$ map is sampled with 128×128 pixels. In order to increase the statistics, for each cluster we produced 29 maps at different projections rotating the cluster around its centre.

3 THE PROPOSED METHOD

The end-to-end pipeline is composed of two main parts: an auto-encoder and an RF regressor. The idea is to extract the features from the SZ images in an unsupervised manner and then to feed the obtained representation to an algorithm which learns how to predict the mass profiles. More details about the architecture can be found hereafter in the text, while the high-level architecture is shown in Fig. 2.

3.1 Auto-encoder for dimensionality reduction

An auto-encoder is a neural network that tries to define a mapping between input $\mathbf{X}$ and an output (reconstruction) $\hat{\mathbf{X}}$ through an internal

Downloaded from https://academic.oup.com/mnras/article/520/3/4000/7024857 by Universita' degli Studi Roma La Sapienza user on 19 June 2023

representation $\mathbf{Z}$, that has a dimension, d, smaller than the input one, $d_{\rm in}$, (Goodfellow, Bengio & Courville 2016) and is used to learn useful properties of the data in an unsupervised setting. It is composed of two parts: the encoder (mapping $\mathbf{X}$ to $\mathbf{Z}$: $\mathbf{Z} = f(\mathbf{X})$) and the decoder (mapping $\mathbf{Z}$ to $\hat{\mathbf{X}}$: $\hat{\mathbf{X}} = g(\mathbf{Z})$). Recently, auto-encoders have been used in astrophysics for different purposes, e.g. generative method of mock SZ observations (Rothschild et al. 2022) and automatic morphological classification of galaxies (Zhou et al. 2022).

In our contest, we set an auto-encoder to derive a representative feature vector with a reduced dimension of our input data, i.e. the SZ maps, while being faithful to the original input. In particular, we build the encoder and decoder steps as follows:

(i) **Encoder** $\{E\}$: $X^{d_{\rm in}} \rightarrow Z^{d}$: it projects the input map $\mathbf{X_{SZ}}$ of dimension $d_{\rm in}$ to a corresponding space through many stacked convolution-batch-normalization-ReLu layers. The output of each encoder is a d-dimensional vector $\mathbf{Z}$ that will be further used by the downstream task algorithm to infer the mass profiles. We note that $d \leq d_{\rm in}$ since the encoder's role is the dimensionality reduction. In our architecture, the encoder is constituted by four layers that project the $d^{\rm in} = 128 \times 128$ SZ maps into a latent vector of dimension $d = 150$.

(ii) **Decoder** $\{D\}$: $Z^{d} \rightarrow X^{d_{\rm in}}$: it has a mirrored architecture to the encoder E (four layers). It takes a vector from the latent space of dimension $d = 150$ and generates the corresponding map $\hat{\mathbf{X}}_{\mathbf{SZ}}$ of dimension $d_{\rm in} = 128 \times 128$. Both networks E and D are trained using a reconstruction loss that catches the difference between the reconstructed map $\hat{\mathbf{X}}_{\mathbf{SZ}}$ and the original one $\mathbf{X_{SZ}}$.

Thus, with this architecture, it acts as a self-supervised feature extractor. For coding the auto-encoder architecture, we made used of the publicly available PYTORCH[1] package (Paszke et al. 2017).

3.2 Random forest method

An RF (Breiman 2001) is a supervised learning algorithm composed by a collection of decision trees. Each tree is an algorithm that is capable of performing classifications or regressions by entering as input some features and by applying a series of if-then-else statements until the possible conditions are fulfilled. Although decision trees are a powerful tool, over time they have proven to be not very flexible and prone to overfitting. The combination of several trees in an RF overcomes these problems (Segal 2003). This is achieved by assigning to each tree a subset of original data by bootstrap sampling and then all the predictions of the individual tree are averaged in the final result. This technique, known as 'bagging', makes RF a robust and versatile model with low variance and less overfitting.

In this work, we use the class RANDOMFORESTREGRESSOR implemented in the python package SCIKIT-LEARN (Pedregosa et al. 2011). In the RF set-up phase, we setup the hyperparameters of the function in order to optimize the performance of the model. According to Fernández-Delgado et al. (2014) and Bentéjac, Csörgö & Martínez-Muñoz (2020), we identify the number of trees, N_ESTIMATORS, as the most important hyperparameter, and the maximum depth of each tree, MAX_DEPTH, as the second. We observe that we reach convergence for N_ESTIMATORS ≥ 200 regardless of the depth of the trees. Regarding the depth, we obtain the best results with the default value of the MAX_DEPTH parameter. Consequently, we set the RF with 200 trees and all other hyperparameters to default values of the RANDOMFORESTREGRESSOR function.

[1] https://pytorch.org

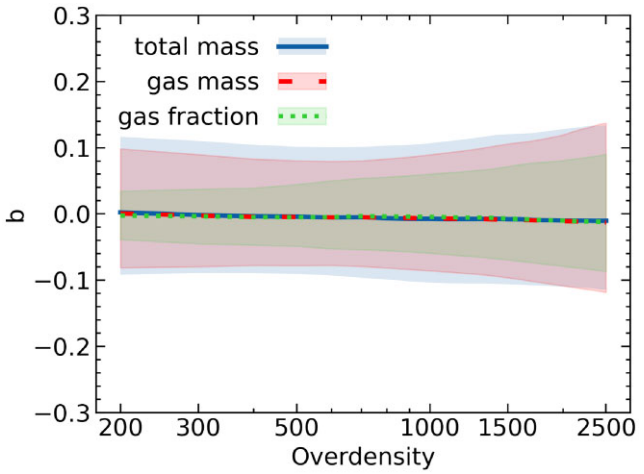

Figure 3. The median bias as a function of the overdensity for total mass (blue solid line), gas mass (red dashed line), and gas fraction (green dotted line). The shaded light blue, pink, and green regions correspond to the 16th–84th percentiles for total, gas mass, and gas fraction, respectively.

3.3 Train and test sets split

Once the RF has been planted, we train it to predict the radial total and gas-only mass profiles from the information extracted from the SZ maps by the auto-encoder algorithm. Therefore, we perform a random selection of the training and test sets containing 80 per cent and 20 per cent of the original sample of 2522 clusters, respectively. Subsequently, we increase the statistics of the two sets by taking into account the 29 projections for each cluster. We have thus ensured that the same cluster cannot belong to different data sets at the same time. Although the mass profiles are extracted from 3D distributions and are common to each projection in both the training and test phases, each projection was treated as independent. This was possible because the starting features are the information extracted from the auto-encoder that are different for each map and for each projection.

4 RESULTS

In this section, we present the application of the trained RF on the test set and the accuracy of its predictions.

We analyse the performance of our model by comparing the predicted and the true profiles at each overdensity. We analyse the performance of our model by comparing the predicted profiles and the true one of the test set, at each overdensity. To perform this task, we define the bias at each Δ as

$$b_{\Delta} = \frac{M_{\Delta}^{\rm pred} - M_{\Delta}^{\rm true}}{M_{\Delta}^{\rm true}}. \quad (3)$$

The biases in the cluster mass estimate after the training of our algorithm is shown in Fig. 3, where the median bias b is evaluated as a function of the overdensities for total and gas masses, represented with blue solid line and red dashed line, respectively. The masses predicted by the RF model are unbiased in the whole range of overdensities, from the cluster core to the outskirts. The median values increase towards the centre but always less than $\sim$1 per cent. The scatter, quantified with the 16th and the 84th percentiles and

Downloaded from https://academic.oup.com/mnras/article/520/3/4000/7024857 by Universita' degli Studi Roma La Sapienza user on 19 June 2023

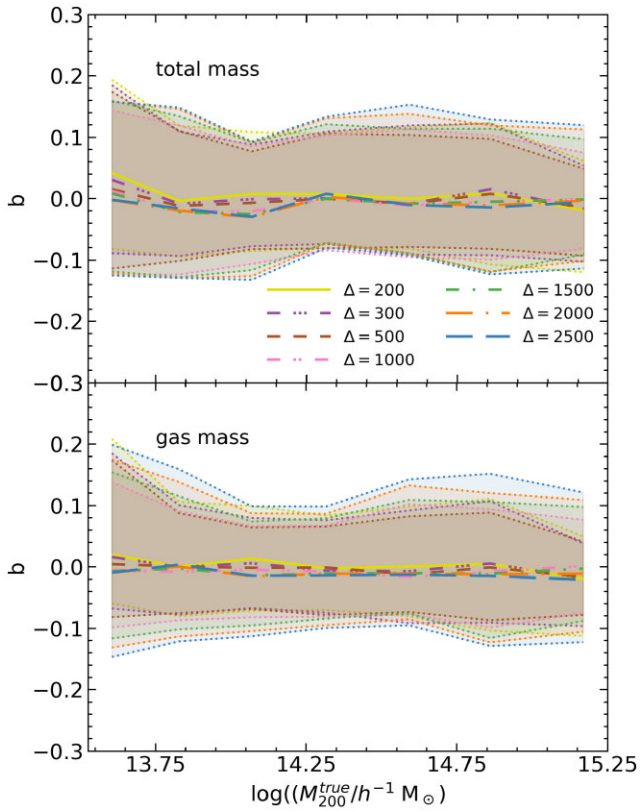

Figure 4. The median bias of the predicted total (upper panel) and gas (lower panel) as a function of the logarithm of true mass $M_{200}^{\rm true}$. For graphical reasons, we only show the lines representing the bias at $\Delta = 200$, 300, 500, 1000, 1500, 2000, and 2500 in yellow, purple, brown, pink, green, orange, and blue, respectively. The shaded areas correspond to the 16th–84th percentiles intervals.

shown with the shaded regions, is around 10 per cent for the total mass (blue) and ∼8 per cent for the gas mass (red). Moreover, the scatter is not properly constant, but become slightly larger in the direction of the cluster outskirts and towards the cluster centre. The minimum scatter is reached for overdensities around 500 and 600 for total and gas profiles, respectively.

The bias for the gas fraction, defined as $(f_{\rm gas}^{\rm pred} - f_{\rm gas}^{\rm true})/f_{\rm gas}^{\rm true}$, is less than 1 per cent in the entire overdensities range considered in this analysis. In this case, the scatter decreases from ∼10 to ∼3 per cent, as shown with the green dotted line in Fig. 3.

4.1 Bias dependence on the total cluster mass

To test if the performance of our ML model suffers of any particular bias related to the true cluster total mass, $M_{200}^{\rm true}$, we study the mass dependence of ML predictions dividing the sample in seven equally populated mass bins. We show in Fig. 4 the median and relative scatter of the total (upper panel) and gas (lower panel) biases for seven chosen overdensities (for graphical reasons). In general, we do not observe any dependence of gas mass profile on cluster true masses in the whole range of overdensities considered. Whereas, we see a tendency to overestimate the total mass in the first mass bin ($10^{13.5} \leq M_{200}^{\rm true}/\,h^{-1}\,{\rm M}_\odot < 10^{13.7}$) for overdensity $\Delta = 200$ and 300. The scatter is around 10 per cent but tends to increase in the low-mass bins for both total and gas profiles.

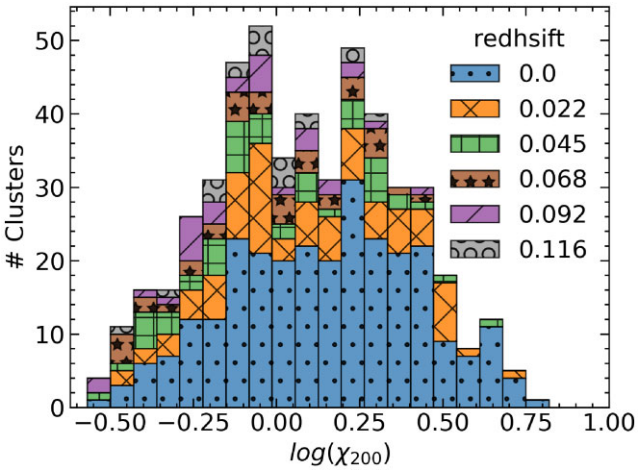

Figure 5. Classification of the dynamical state of the clusters within the test sample in terms of the relaxation parameter χ_{200}. The blue bars represent zero redshift clusters, while higher redshift clusters are represented by the coloured bars according to the legend.

4.2 Bias dependence on dynamical state

Classical methods to infer the cluster mass from SZ and X-ray observations make assumptions on the hydrostatic equilibrium of the clusters, so they are sensitive to deviation from it (e.g. Ruppin et al. 2018; Pearce et al. 2019; Gianfagna et al. 2021). Therefore, it is extremely important to investigate if and how the performance of our ML approach change with the dynamical state of the clusters. Considering hydrodynamical simulation, it is possible for a specific cluster to extract any possible dynamical or thermodynamical information about its components, like particle 3D velocity, entropy, etc. Based on these information, several indicators have been defined in the literature to assess the dynamical state of synthetic clusters. In this work, we use the relaxation parameter χ originally introduced in Haggar et al. (2020) and later revised in De Luca et al. (2021), combining only two indicators:

$$\chi_{200} = \sqrt{\frac{2}{\left(\frac{f_s}{0.1}\right)^2 + \left(\frac{\Delta_r}{0.1}\right)^2}}, \tag{4}$$

where f_s is the ratio between the sum of the masses of all the subhaloes within R_{200} and the cluster total mass M_{200}, and Δ_r is the offset between the theoretical centre of the cluster and the centre of mass of the cluster, normalized to R_{200}. The distribution of our sample as a function of the relaxation parameter is shown in Fig. 5, here negative and positive tails represent extremely disturbed and extremely relaxed systems, respectively.

The median biases are shown in Fig. 6 for seven equally populated bins of χ_{200}. Only seven overdensities are plotted for clarity. We see that in general, the model is sensitive to the dynamical state of the clusters. There is a dependence of both total (upper panel) and gas (lower panel) mass reconstruction with the dynamical state, depending also on the overdensity. Our ML analysis tends to underestimate the mass in the outskirts of disturbed clusters and to overestimate it in the inner part, while it behaves in the opposite for relaxed systems. However, profiles at $\Delta = 500$ and 600 do not show any dependence on χ_{200}. This behaviour, as a function of the dynamical state, can also explain the minimum of the scatter around these overdensities that we observed in Fig. 3. Regarding the scatter, it remains ∼10 per cent for $\log(\chi) > 0$ at all the overdensities. For $\log(\chi) < 0$, the scatter starts to grow as the clusters become

Downloaded from https://academic.oup.com/mnras/article/520/3/4000/7024857 by Universita' degli Studi Roma La Sapienza user on 19 June 2023

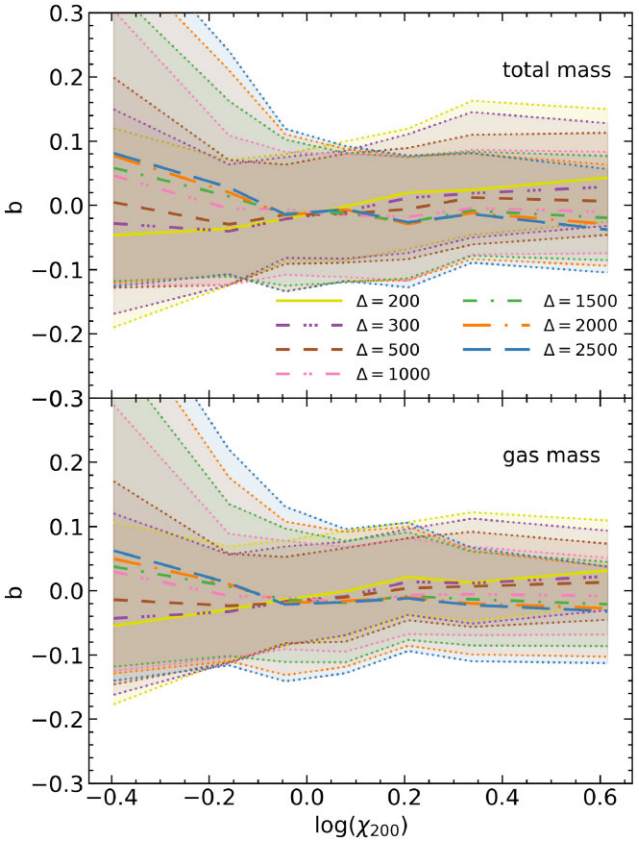

Figure 6. The median bias of the predicted total (upper panel) and gas (lower panel) mass with respect $M_{\rm true}$ as a function of the logarithm of the relaxation parameter χ_{200}. For graphical reasons we only show the lines representing the bias at $\Delta = 200$, 300, 500, 1000, 1500, 2000, and 2500 in yellow, purple, brown, pink, green, orange, and blue, respectively. The shaded areas correspond to the 16th–84th percentiles intervals.

more disturbed. Moreover, we see that the scatter remains around 15 per cent for overdensities related to the cluster outskirts, whereas it grows up to ∼30 per cent going towards clusters' inner regions.

5 THE CONCENTRATION–MASS RELATION FROM INFERRED PROFILES

Investigating the mass profile provides more information on the galaxy cluster internal structure. A general, good tracer of the mass profile of galaxy clusters is given by the two-parameter Navarro–Frenk–White (NFW) model (Navarro, Frenk & White 1997). Besides the enclosed masses estimated at different overdensities, we examine whether the profiles from these masses give consistent NFW concentration parameters. In this section, we fit the predicted profiles with 24 different data points (overdensities) to the NFW profile and derive the $c_{\rm ML} = R_{200}/r_s$, where r_s is the typical scaling radius of the NFW profile. Thus, we compare these estimates with the concentration parameters, $c_{\rm true}$, calculated using the true mass profiles.

In Fig. 7, we show both $c_{\rm true}$ (cyan squares) and $c_{\rm ML}$ (magenta cycles) as a function of the true halo mass $M_{200}^{\rm true}$. The errorbars for the $c_{\rm ML}$ data (magenta circles) represent 16th–84th percentiles among the 29 projections. The concentration–mass relation, represented by the blue triangles and red stars, is obtained by computing the median of $c_{\rm true}$ and $c_{\rm ML}$ in seven equally populated mass bins, respectively. The relations of our ML analysis and the true one are almost

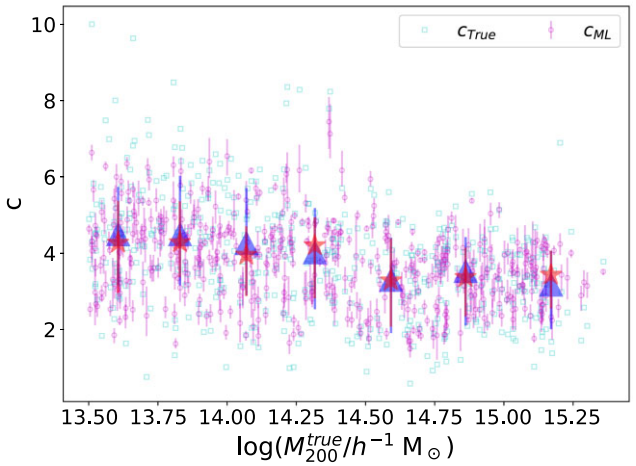

Figure 7. The concentration–halo mass relation from both the true profiles, denoted by $c_{\rm true}$, and the ML profiles $c_{\rm ML}$. The blue triangles and red stars show the median concentrations for $c_{\rm true}$ and $c_{\rm ML}$, respectively, within the halo mass bins. Error bars show the 16th–84th percentiles. Magenta circles with error bars show the median value with 16th–84th percentiles of the 29 projections.

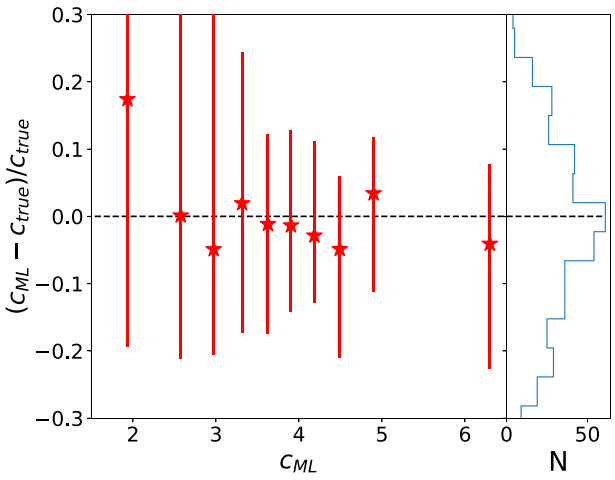

Figure 8. The concentration bias as a function of $c_{\rm ML}$ from the predicted halo profile. Here, we only show the median values and 16th–84th percentiles in each concentration $c_{\rm ML}$ bin that contains the same number of clusters per bin. Thus, a slight difference in bin size is expected. Here, $c_{\rm ML}$ means the median result of concentration from the 29 projected maps per cluster. The right-hand side panel shows the overall distribution of the concentration bias.

indistinguishable, whereas the errorbars (16th–84$^{\rm th}$ percentiles) in the ML c–M relation are slightly smaller than the true ones. In general, the predicted concentration has small scatters with respect to the true one, which means a small projection effect for these $c_{\rm ML}$. Therefore, the extreme concentration values at both $c \lesssim 1$ and $c \gtrsim 7$ are less represented.

We further quantify the concentration bias ($c_{\rm ML}/c_{\rm true} - 1$) in Fig. 8 as a function of the predicted median concentration, $c_{\rm ML}$, over the 29 projections.

After dividing the sample into 10 bins of $c_{\rm ML}$ with the same number of clusters, the median concentration bias wiggles around 0, except at the lowest concentration bin. However, it is worth noting that the error bars at low concentrations are larger compared to those of

Downloaded from https://academic.oup.com/mnras/article/520/3/4000/7024857 by Universita' degli Studi Roma La Sapienza user on 19 June 2023

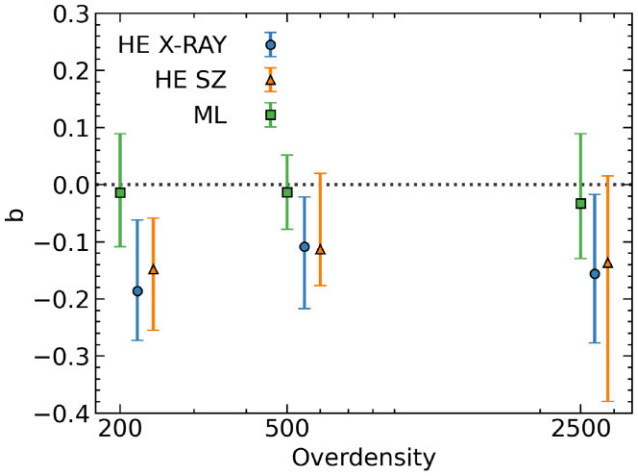

Figure 9. Median bias estimated with ML method compared with HE mass bias values at the three common overdensities for the same cluster selection in THE THREE HUNDRED sample at $z = 0$ analysed in Gianfagna et al. (2022). The error bars represent 16th–84th percentiles.

mass biases (Fig. 4), while they are comparable at intermediate and high concentrations. Instead, we see that this trend is similar to the one shown in Fig. 6. We speculate that a possible explanation for this behaviour is that ML tends to overpredict the masses at higher overdensities (see Fig. 6) for dynamical unrelaxed clusters caused by major merger events that, instead, tend to have lower concentrations. Therefore, the concentration of ML profiles is biased high for objects with low concentrations, while ML underpredicts their masses in the core, which results in a slightly lower concentration. This picture is consistent with having fewer outliers from the ML results, as shown in Fig. 7.

6 COMPARISON WITH HE MASS ESTIMATES

Our ML model recovers the mass radial profiles with median bias close to zero. It is remarkable that we achieve this result without making any a priori assumption on the physical properties of the clusters. Here, we compare our median bias with the mass bias computed when HE approximation is adopted. We refer to the analysis of Gianfagna et al. (2022) where also synthetic clusters from THE THREE HUNDRED have been used. The mass of the clusters was inferred by using ICM data typical of X-ray and SZ observations. Only the most massive clusters present in each resimulated region at redshift $z = 0$ were considered. In order to compare our result with them, we recalculated the bias only for the common clusters, 53 objects in a mass range between 1.3×10^{14} and $3 \times 10^{15}\ h^{-1}\,\mathrm{M}_{\odot}$. The results of this comparison are shown in Fig. 9. The HE bias is of the order of 10−20 per cent considering X-ray observables (red dots) such as electron gas temperature and density or SZ (green)-derived pressure and density. In the case of ML estimates (blue dots), it is clear that the bias is less than 1 per cent with a scatter of approximately 10 per cent. Interestingly, the bias shows the lower scatter at $\Delta = 500$. Although the biases are compatible within the errors, ML mass estimates are systematically more accurate and unbiased than the HE ones. Moreover, the ML approach results in a smaller scatter in the whole range of overdensities.

7 CONCLUSIONS

Only recently, cluster masses have been recovered with ML approaches starting from different spectral band images but always at one specific single aperture, such as M_{200} or M_{500}. In this paper, we present an ML model that for the first time is able to infer simultaneously the full integrated radial profile for the gas and the total mass from SZ mock images. The ML model architecture is a combination of an auto-encoder and an RF regressor. This ML algorithm is trained and tested on a sample of 73 138 mock Compton-y parameter maps generated along 29 projections for each of the 2522 galaxy clusters extracted from the GADGET-X run of THE THREE HUNDRED simulations.

The auto-encoder is used to encrypt the relevant information from each map, while the RF performs the final estimation of the radial mass profiles. The model is able to infer the gas mass profile, responsible for the SZ effect signal in the maps, but also the cluster total mass without any a priori assumption on the hydrostatic equilibrium of the cluster.

Our main results can be summarized as follows:

(i) The ML model is able to recover unbiased profiles (bias lower than 1 per cent) with a scatter of ∼10 per cent that is slightly increasing towards the outskirts and to the inner part of the cluster (Fig. 3) with a minimum of around an overdensity of $\Delta \sim 600$.

(ii) The accuracy and the precision of the method do not depend on the cluster mass (Fig. 4). Nevertheless, they are more affected by the dynamical state with an impact that depends on the overdensity. In general, the scatter increases in unrelaxed clusters due to projection effects.

(iii) From the total and gas mass profiles, we also derived the gas fraction profile. The bias, in this case, is also lower than 1 per cent, while the scatter decreases up to ∼3 per cent in the outskirts.

(iv) The concentration parameter, obtained by fitting the inferred total mass profiles with an NFW model, seems to be unbiased with a scatter between 10 and 20 per cent for $c_{\mathrm{ML}} > 2$. Therefore, the ML-predicted c–M relation is in reasonable agreement with the true one.

(v) The comparison with a standard method to infer the cluster total mass, such as the HE approximation, shows that our estimation of the mass is more accurate as it does not suffer from the hydrostatic mass bias.

Furthermore, in order to make this approach less prone to the physical models implemented in the simulation, we investigated the possibility of training the model with data from different simulations, such as GADGET-X (AGN feedback) and GIZMO-SIMBA (strong AGN feedback). As described in Appendix A, the network trained in this way is able to marginalize over different hydrodynamical simulations, obtaining results that are compatible with single-simulation training. Therefore, for future applications, we are going to use this kind of approach by further extending the data set with other simulations in order to marginalize over all possible baryonic effects.

The framework presented in this paper can be extended to also infer other ICM radial profiles such as gas temperature and pressure, among others. Its application on different observational maps, such as optical and X-ray mock images, seems a promising way to improve the reconstruction of these profiles.

In a forthcoming paper, we plan to train this ML approach on mock SZ maps, adding instrumental and observational effects, such as noise and limited angular resolution. Then, the model will be tested

Downloaded from https://academic.oup.com/mnras/article/520/3/4000/7024857 by Universita' degli Studi Roma La Sapienza user on 19 June 2023

on real Compton-y parameter maps at different angular resolutions and at different redshifts. Nevertheless, the redshift evolution of the Y–M relation is negligible or weak up to $z = 1$ (Henden, Puchwein & Sijacki 2019; de Andres et al. 2023). The bias in the inferred ML mass will also be compared with other methods using weak lensing mock images of the same cluster data set.

ACKNOWLEDGEMENTS

We thank the anonymous referee for his/her valuable suggestions and comments. Most of the simulations used in this work have been performed in the MareNostrum Supercomputer at the Barcelona Supercomputing Center, thanks to CPU time granted by the Red Española de Supercomputación. AF, AS, and MDP acknowledge support from Sapienza Università di Roma, thanks to Progetti di Ricerca Medi 2019, RM11916B7540DD8D and 2021, RM12117A51D5269B. AF also thanks financial support by Universidad de La Laguna (ULL), NextGenerationEU/PRTR, and Ministerio de Universidades (MIU) (UNI/511/2021) through grant 'Margarita Salas'. DdA, WC, and GY acknowledge Ministerio de Ciencia e Innovación (Spain) for partial financial support under research grant PID2021-122603NB-C21. WC was also supported by the STFC AGP grant ST/V000594/1 and the Atracción de Talento Contract no. 2020-T1/TIC-19882 granted by the Comunidad de Madrid in Spain. He further acknowledges the science research grants from the China Manned Space Project with nos. CMS-CSST-2021-A01 and CMS-CSST-2021-B01.

DATA AVAILABILITY

The data used in this paper are part of THE THREE HUNDRED project and can be accessed following the guidelines that can be found in the main website[2] of the collaboration. The data specifically shown in this paper will be shared upon request to the authors.

REFERENCES

Allen S. W., Evrard A. E., Mantz A. B., 2011, ARA&A, 49, 409
Ansarifard S. et al., 2020, A&A, 634, A113
Baldi A. S., De Petris M., Sembolini F., Yepes G., Cui W., Lamagna L., 2018, MNRAS, 479, 4028
Beck A. M. et al., 2016, MNRAS, 455, 2110
Behroozi P. S., Wechsler R. H., Wu H.-Y., 2013, ApJ, 762, 109
Bentéjac C., Csörgö A., Martínez-Muñoz G., 2020, Artif. Intell. Rev., 54, 1937
Breiman L., 2001, Mach. Learn., 45, 5
Cui W. et al., 2018, MNRAS, 480, 2898
Cui W. et al., 2022, MNRAS, 514, 977
de Andres D. et al., 2022, Nat. Astron., 6, 1325
de Andres D., Yepes G., Sembolini F., Martínez-Muñoz G., Cui W., Robledo F., Chuang C.-H., Rasia E., 2023, MNRAS, 518, 111
De Luca F., De Petris M., Yepes G., Cui W., Knebe A., Rasia E., 2021, MNRAS, 504, 5383
Fernández-Delgado M., Cernadas E., Barro S., Amorim D., 2014, J. Mach. Learn. Res., 15, 3133
Gianfagna G. et al., 2021, MNRAS, 502, 5115
Gianfagna G., Rasia E., Cui W., De Petris M., Yepes G., 2022, in EPJ Web Conf., 257, 00020
Goodfellow I. J., Bengio Y., Courville A., 2016, Deep Learning. MIT Press, Cambridge
Gupta N., Reichardt C. L., 2020, ApJ, 900, 110
Gupta N., Reichardt C. L., 2021, ApJ, 923, 96
Haggar R., Gray M. E., Pearce F. R., Knebe A., Cui W., Mostoghiu R., Yepes G., 2020, MNRAS, 492, 6074
Henden N. A., Puchwein E., Sijacki D., 2019, MNRAS, 489, 2439
Henson M. A., Barnes D. J., Kay S. T., McCarthy I. G., Schaye J., 2016, MNRAS, 465, 3361
Ho M., Rau M. M., Ntampaka M., Farahi A., Trac H., Póczos B., 2019, ApJ, 887, 25
Klypin A., Yepes G., Gottlöber S., Prada F., Heß S., 2016, MNRAS, 457, 4340
Knollmann S. R., Knebe A., 2009, ApJS, 182, 608
Kravtsov A. V., Borgani S., 2012, ARA&A, 50, 353
Lau E. T., Kravtsov A. V., Nagai D., 2009, ApJ, 705, 1129
Le Brun A. M. C., McCarthy I. G., Melin J.-B., 2015, MNRAS, 451, 3868
Navarro J. F., Frenk C. S., White S. D. M., 1997, ApJ, 490, 493
Ntampaka M., Trac H., Sutherland D. J., Battaglia N., Póczos B., Schneider J., 2015, ApJ, 803, 50
Ntampaka M., Trac H., Sutherland D. J., Fromenteau S., Póczos B., Schneider J., 2016, ApJ, 831, 135
Ntampaka M., Trac H., Cisewski J., Price L. C., 2017, ApJ, 835, 106
Ntampaka M. et al., 2019, ApJ, 876, 82
Paszke A. et al., 2017, Automatic differentiation in PyTorch, NIPS 2017 Workshop on Autodiff, Long Beach, California
Pearce F. A., Kay S. T., Barnes D. J., Bower R. G., Schaller M., 2019, MNRAS, 491, 1622
Pedregosa F. et al., 2011, J. Mach. Learn. Res., 12, 2825
Planck Collaboration XIII, 2016, A&A, 594, A13
Pratt G. W., Arnaud M., Biviano A., Eckert D., Ettori S., Nagai D., Okabe N., Reiprich T. H., 2019, Space Sci. Rev., 215, 25
Rothschild T., Nagai D., Aung H., Green S. B., Ntampaka M., ZuHone J., 2022, MNRAS, 513, 333
Ruppin F. et al., 2018, A&A, 615, A112
Salvati L., Douspis M., Aghanim N., 2020, A&A, 643, A20
Segal M., 2003, Technical Report, Center for Bioinformatics and Molecular Biostatistics. University of California, San Francisco
Sembolini F., Yepes G., De Petris M., Gottlöber S., Lamagna L., Comis B., 2013, MNRAS, 429, 323
Sereno M., Ettori S., 2017, MNRAS, 468, 3322
Springel V., 2005, MNRAS, 364, 1105
Springel V., Hernquist L., 2003, MNRAS, 339, 289
Steinborn L. K., Dolag K., Hirschmann M., Prieto M. A., Remus R.-S., 2015, MNRAS, 448, 1504
Sunyaev R. A., Zeldovich Y. B., 1970, Ap&SS, 7, 3
Tornatore L., Borgani S., Dolag K., Matteucci F., 2007, MNRAS, 382, 1050
Villaescusa-Navarro F. et al., 2021, ApJ, 915, 71
Wicker R., Douspis M., Salvati L., Aghanim N., 2022, EPJ Web Conf., 257, 00046
Yan Z., Mead A. J., Van Waerbeke L., Hinshaw G., McCarthy I. G., 2020, MNRAS, 499, 3445
Zhou C., Gu Y., Fang G., Lin Z., 2022, AJ, 163, 86

APPENDIX A: IMPACT OF MULTISIMULATION TRAINING

In Sections 2 and 3, we described that the proposed network was trained with cluster maps selected within the GADGET-X run of THE THREE HUNDRED project simulation. In Section 4 we showed the quality of the results obtained on a test set composed of clusters selected from the same simulation. However, each simulation has its own characteristics such as cosmology, resolution, or different baryonic physics. These differences can have effects of greater or lesser importance on e.g. the mass of the structures, the shape of the mass profiles, or the SZ maps. For this reason, if the differences between the products of different simulations are significant, the accuracy of ML or more classical methods, such as scaling relations, may be compromised. In the context of machine learning, to overcome this problem one possible approach is to train a network with

[2] https://the300-project.org

Downloaded from https://academic.oup.com/mnras/article/520/3/4000/7024857 by Universita' degli Studi Roma La Sapienza user on 19 June 2023

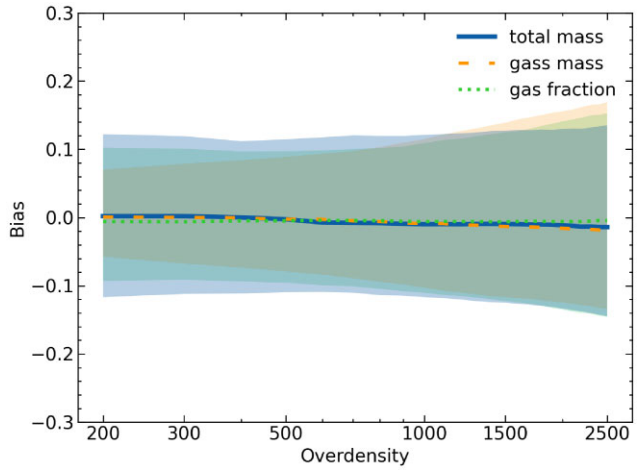

Figure A1. The median bias of a sample of clusters selected from both GADGET-X and GIZMO-SIMBA as a function of the overdensity for total mass (blue solid line), gas mass (orange dashed line), and gas fraction (green dotted line). The shaded light blue, orange, and green regions correspond to the 16th–84th percentiles for total, gas mass, and gas fraction, respectively.

the products of different simulations as proposed by the Cosmology and Astrophysics with MachinE Learning Simulations (CAMELS; Villaescusa-Navarro et al. 2021). Following this approach, we decided to re-train our model by adding to the clusters selected from the GADGET-X run those produced by the GIZMO-SIMBA run (for details on the two runs, see Cui et al. 2022).

Fig. A1 shows that using the network to predict the mass profiles of a test set consisting of a mixture of clusters from GADGET-X and GIZMO-SIMBA yields results that are completely in line with what was obtained with the network trained and tested on GADGET-X clusters alone, i.e. the median bias of both mass profiles is zero and the scatter is about 10 per cent for all overdensities.

The most interesting results are those obtained by applying this network to test sets consisting of clusters from each run separately. In the case of the test set of only GADGET-X clusters (top panel of Fig. A2), the median bias of the predicted total mass profiles (blue solid line) is zero, and the scatter (blue shaded region) is also perfectly in accordance with what was achieved with the network trained with only GADGET-X clusters. On the other hand, regarding the gas mass profiles (orange dashed line), we observe a bias that slightly decreases to ~ -5 per cent towards the cluster core whereas the scatter remains similar to that of the previous cases. In the bottom panel of Fig. A2, we show the results of the network applied to the GIZMO-SIMBA clusters. In this case, the median bias of the total mass profiles is zero up to $\Delta \leq 500$ and then it grows to about 5 per cent in the core. The scatter grows slightly but remains below 20 per cent. The gas mass profiles show a fairly constant bias around 3 per cent, moreover, for these profiles the scatter increases significantly in the inner part of the clusters. This might be caused by the strong AGN-feedback implemented in GIZMO-SIMBA. In contrast, GADGET-X predictions are more stable in the centre.

In conclusion, the approach of training the network with a mixture of clusters from different simulations gives accurate results in estimating the profiles of the two tests separately, showing the flexibility of our ML model. Differences, as might be expected, are observed for the gas mass profiles as well as in the innermost part of the clusters where the different baryon physics models have greater effects.

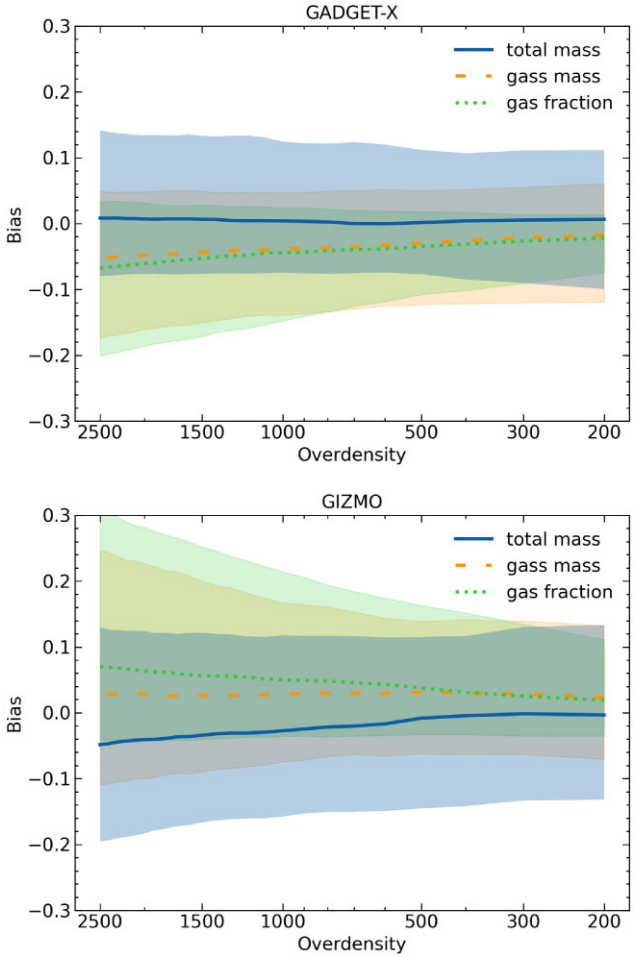

Figure A2. The median bias of GADGET-X (top panel) and GIZMO-SIMBA (bottom panel) clusters as a function of the overdensity for total mass (blue solid line), gas mass (red dashed line), and gas fraction (green dotted line). The shaded light blue, pink, and green regions correspond to the 16th–84th percentiles for total, gas mass, and gas fraction, respectively.

This paper has been typeset from a TEX/LATEX file prepared by the author.

Downloaded from https://academic.oup.com/mnras/article/520/3/4000/7024857 by Universita' degli Studi Roma La Sapienza user on 19 June 2023